ATMOSPHERIC PHASE NOISE AND APERTURE SYNTHESIS IMAGING AT MILLIMETER WAVELENGTHS

M. C. H. Wright
Radio Astronomy laboratory, University of California, Berkeley, CA, 94720

ABSTRACT

We analyse data obtained with the Hat Creek interferometer at 86 GHz to estimate the atmospheric phase noise on spatial scales of 6m to 846m, and time scales of 1 second to 10 hours. We find a phase structure function with a power law index, β between 0.6 and 1.7. A slope close to the Kolmogorov 2D value 0.67 is obtained for longer baselines and stable weather conditions; the slope approaches the Kolmogorov 3D value 1.67 only on short baselines and in turbulent weather. The rms phase at a 1 km baseline is 1 mm, with a variation by a factor 4 over a few days even during good weather conditions. The mean elevation dependence is sin(elevation) $^{-0.7+/-0.2}$. The variation of β and the elevation dependence with baseline length are consistent with turbulent regions 100 - 300 m thick.

The resolution and dynamic range of millimeter wavelength aperture synthesis images is limited by atmospheric turbulence. Observing techniques and data analysis procedures to correct for atmospheric seeing are discussed in some detail.

1. Introduction

Atmospheric turbulence creates refractive index variations which limit the resolution and sensitivity of observations of astronomical sources. At optical wavelengths, the seeing is limited by tropospheric density fluctuations with typical size 10 cm, and time scales of 10 msec. At radio wavelengths, the refractive index of water vapour is 20 times larger than at optical wavelengths and fluctuations in the water vapour are more important. At wavelengths longer than 30 cm, fluctuations in the ionosphere limit the resolution. (See Baldwin and Wang, 1990, for a recent review of radio seeing, and Masson, 1994a, for a comparison of optical and radio seeing.) At millimeter wavelengths, refractive index fluctuations are expected to be dominated by water vapour variations which are coupled through temperature and relative humidity to the velocity field. Refractive index fluctuations inferred from interferometer phase measurements have been observed with sizes from 1m to 10 km, and persistence times from 0.1s to several hours.

The wavefront from a radio source is distorted by atmospheric refractive index variations, which results in phase variations across the telescope aperture. An interferometer array directly observes the path difference through the atmosphere between the two antennas on each baseline.

Fluctuations on a larger scale than the antenna separation are partially correlated at each antenna, and the interferometer phase fluctuations are reduced on short baselines.

The phase structure function (PSF), $D\phi(b, T)$, is used to measure the phase fluctuations as a function of the time interval between samples, T, and separation between antennas, b.

$$D\phi(b, T) = < (\phi(x, t) - \phi(x + b, t + T))^2 > \tag{1}$$

The phase structure function is assumed to be isotropic. For three dimensional, Kolmogorov turbulence , the structure function follows a power law b^β with a slope $\beta = 5/3$ for values of b between an outer scale, L, where energy is deposited into the medium, and an inner scale, l, where the energy is dissipated (Kolmogorov, 1941). On spatial scales larger than the thickness of the turbulent region, the turbulence is expected to become two-dimensional and the structure function scales as $b^{2/3}$ (Tatarskii, 1961). Under the Taylor hypothesis, the bulk velocity of the turbulent pattern is larger than the internal velocities, and the time variation follows the same power law with $t = b/v$, where v is the drift velocity of the the turbulence past the telescopes. (Taylor, 1938)

Model atmosphere calculations by Treuhaft and Lanyi (1987) predict a smooth transition from a 5/3 power law at baselines small compared to the scale height of the water vapour, to a 2/3 power law at large antenna separations. The scale height of the water vapour is about 2 km (Thompson, Moran, and Swenson, 1986); at longer baselines the fluctuations increase slowly with baseline length. On very long baselines, for example in VLBI experiments, the fluctuations are independent of baseline length since the variation with baseline length is not detectable in typical experiments; observations over several days would be required to observe the fluctuations corresponding to the passage of weather systems.

Observations of radio seeing have found a wide range of slopes, β, mostly falling between 2/3 and 5/3, and consistent with the Kolmogorov-Taylor theory. Observations at 5 GHz with the VLA on baselines 1-35 km (Armstrong and Sramek, 1982) found $\beta = 1.4$ in reasonable agreement with Kolmogorov theory for 3D turbulence, although the baselines involved were larger than the scale height of the troposphere, and hence larger than the expected outer scale. More recent analysis of a large set of VLA data at 5 and 15 GHz (Sramek, 1990) found a median value $\beta =$ 0.68. From an analysis of stellar scintillation, Coulman and Vernin (1991) propose an outer scale as small at 5m, with a shift from a Kolmogorov 5/3 index, through a "spectral gap" from 5 - 1200m, and a Kolmogorov 2/3 index at baselines greater than 1200 m. Observations at 10 microns show significant departures from the Kolmogorov model; under good seeing conditions the phase structure function of time is proportional to the time interval – a random walk process (Bester etal. 1992).

Atmospheric phase fluctuations scale with frequency, and become an important factor in the design and operation of millimeter arrays (e.g. Holdaway 1992a). If uncorrected, phase fluctuations limit the resolution to about 0.5 arcsecond at 3mm wavelength (Bieging etal, 1984), and 1 arcsecond at 1mm (Olmi & Downes, 1992). Poorer resolution will be obtained at shorter wavelengths since the phase fluctuations scale as $b^{\beta/2}/\lambda$, and hence the seeing limited resolution, scales as $\lambda^{1-2/\beta}$ (Thompson, Moran & Swenson, 1986). Previous observations at millimeter wavelengths (Bieging etal, 1984; Wright and Welch, 1990; Kasuga etal 1986; Olmi & Downes, 1992) covered only a small range of baselines. Until recently, millimeter wavelength aperture synthesis techniques have used the same algorithms developed for centimeter wavelength interferometry, with instrumental gain and phase calibrations at intervals of 15 to 30 minutes. This procedure has worked quite well for baselines less than about 300 m in good weather conditions, but excessive phase noise at longer baselines, or in less perfect weather requires significantly modified observing and data reduction techniques. In this paper we analyse data from the BIMA array on time scales of 1s - 10 hrs and antenna separations from 6 - 846m, and discuss observing techniques and data analysis procedures to correct for atmospheric seeing.

2. Observations

The observations reported here were obtained with the BIMA 6-antenna array during the period 1993 July to 1995 October. Most of the data are a by-product of aperture synthesis observations of the SiO maser emission at 86.243 Ghz from OMC1 in one of the standard array configurations with projected antenna separations ranging from 6 to 846 m. (see Wright et al.,1995; Plambeck et al. 1995). These observations are up to 10 hours in length with integration times 10 to 30s. The SiO maser emission provides a strong signal that clearly differentiates atmospheric effects from instrumental and thermal phase noise. For a single source, errors in the position and instrumental baseline have a 12 hour period and do not contribute to the measured phase noise. Figure 1 shows the interferometer phase for the Orion SiO maser with antenna separations from 97 to 846 m. Fluctuations in the closure phase and in the relative phase of two spectral features centered at -6 and 14 km/s are less than 1 degree of phase in a 15s integration, corresponding to 10 microns of path length at the line frequency. This is consistent with thermal noise from the receiver and atmospheric opacity. The atmospheric phase noise we observed at an 800 m baseline is 100 times the thermal phase noise.

We also made a number of special observations to investigate the atmospheric phase behaviour with integration times as short as 1s, and as a function of source separation, time of year, time of day, wind speed, and humidity. The short integrations were obtained with a fast sampling program designed for solar observing. Most of these observations used a 2s integration time, giving a sample interval 2.3s, and a thermal phase noise 3 degrees on 3c273 in an 800 MHz bandwidth. In order to switch between sources as rapidly as possible, we observed a pair of sources as offset pointing positions in a multi-field (mosaicing) observation. In this way we reduced the system overhead to a minimum and were able to alternate between the quasars 3c273 and 3c279 in 30s, including a 10s integration on source. These observations were also made with an 800 MHz bandwidth, giving a thermal phase noise of around 1 degree in a 10s integration.

For each data set we derived the following quantities: rms phase as a function of baseline length, the Allan deviation, and the temporal spectrum of the phase fluctuations. The total power, air temperature, relative humidity, and wind speed and direction were recorded with most datasets so we were able to investigate the correlations with these parameters.

3. Results

We fitted structure functions of the form

$$rmspath = \sigma \times baseline^{\beta/2} \times sin(elevation))^{-0.5} + noise \tag{2}$$

where σ is the intercept at a 1 km baseline, and β is the slope of the phase structure function for sufficiently long averaging times (see section 4.1). The thermal noise from the electronics, antenna spillover, and atmospheric opacity is insignificant compared with the atmospheric phase noise; varying the noise term from 0 to 10 degrees did not change the results.

For the SiO maser data we computed the rms phase over intervals of 5 min to 135 min. The phase was unwrapped from a -180 to 180 degree interval using a simple nearest neighbor algorithm which was sufficient for this well sampled, high signal to noise data. The best sampled data are listed in Tables 1 and 2. Table 1 shows the fitted rms path at a 1 km baseline, and the slope as a function of the physical baseline length, with the elevation dependence set to sin(elevation) $^{-0.5}$. For the longer datasets, and for the shorter averaging intervals, we were able to fit for the elevation dependence. These fits are shown in Table 2. We tried fitting versus the projected baseline length (as in Bieging etal, 1984; Wright & Welch, 1990; and Olmi & Downes, 1992), and versus the physical baseline length (as in Sramek, 1983; Armstrong and Sramek, 1982; Sramek, 1990). With a small number of antennas a larger sample of baseline lengths is obtained by fitting versus the projected baseline length rather than the physical baseline length. The choice of baseline variable depends on the atmospheric model. For a thin layer of turbulence, the paths to the antennas are separated by the antenna separations, but for a thick layer the separation is the projected baseline. In fact it does not seem to make much difference to the fitted variables. The best sampled data was obtained in the period 14dec94 to 08feb95, with antenna separations from 97 to 846 m, and projected baselines from 60 to 846m. For these 10 runs the mean value of the rms, σ, and slope, $\beta/2$, in a 5 min interval at a 1 km antenna separation is $\sigma_{5min}(1km) = 0.67 \pm 0.15$, and $\beta/2 = 0.36 \pm 0.07$. Using the projected baseline as the independent variable we obtain $\sigma = 0.82 \pm 0.08$,and $\beta/2 = 0.38 \pm 0.03$. The tighter fit using projected baselines might be construed as evidence against a thin turbulent screen. The rms increases with averaging interval roughly as the 1/3 power; β increases slightly. The mean values for the 10 runs are: $\sigma_{15min}(1km) = 0.99 \pm 0.11$, and $\beta/2 = 0.45 \pm 0.07$, $\sigma_{45min}(1km) = 1.50 \pm 0.33$, and $\beta/2 = 0.54 \pm 0.14$. The data are less well sampled for the other data included in Table 1, and the range of baselines is smaller (6 to 52m in 1993 November, 12 to 128m in 1993 December, 31 to 238m in 1994 January, and 12 to 83m in 1995 August). However, as is evident from Tables 1 and

2, smaller values of σ were obtained in the winter of 1993, and much larger values in summer than in winter. The mean values for the winter (October to March), and summer (April to September) are: $\sigma_{15min}(1km) = 0.80 \pm 0.40$, and $\beta/2 = 0.44 \pm 0.11$, and $\sigma_{15min}(1km) = 2.23 \pm 1.21$, and $\beta/2 = 0.67 \pm 0.19$ respectively. The rms phase noise can change by a factor 2 to 3 in a few days. Although the values for σ and β are inversely correlated in the fits, (a high β can compensate for a low σ, and vice-versa), in the best conditions we obtain a low value for both σ and β; in the worst conditions both σ and β increase.

We investigated the correlation of σ and β with humidity and wind speed. Outside of the seasonal variation, there is little correlation of either σ or β with humidity. There is a significant correlation of both with wind speed, which is most evident in typical summer afternoon conditions at Hat Creek. Quantitatively, we have measured a 50% increase in phase noise for a wind increase from 2 to 6 m/s, and an increase in β to 1.7, on baselines less than 40m. We have found little correlation with the wind direction.

For the source switching data we analysed whether the rms phase in one source could be reduced by interpolating the phase from the other. These results are discussed in more detail below.

To verify that the fitted parameters were not generated by some quirk of data sampling or software, we generated several sets of interferometer data with similar sampling to the real data, but with the data replaced by Gaussian additive (thermal) noise, or with Gaussian phase noise, or both. In all cases the result of computing phase structure functions, Allan deviations, and power spectra was to produce zero slopes as a function of baseline, time, or frequency respectively.

4. Discussion

4.1. Phase Structure Function

An interferometer array directly measures the PSF over the range of baselines in the array, without invoking Taylor's hypothesis. The data must be averaged over sufficient time to sample the full range of the fluctuations; usually stated as a few times b/v, where b is the antenna separation, and v the wind velocity. In practice, turbulence is experienced even in extremely low winds, and instrumental phase drifts can increase the measured fluctuation if the interval is too long. Only a mean value was removed in computing the PSF. As noted by Sramek (1990), removing a slope risks lowering the measured turbulence. The largest errors in the values listed in Tables 1 and 2 come from instrumental phase drifts. Instrumental phase drifts due to cable length variations are removed from the data. However, there was a problem with phase drifts on the long baselines which becomes apparent at the longer integration times in Table 1. Instrumental phase drifts on the short baselines were much better controlled. Removing a linear phase slope from the data reduces both the rms and the fitted slope. For averaging times less than 45 min, the changes are typically 2 – 5 percent in σ, and 5 – 10 percent in the slope. For an averaging time of 135 min σ decreases by up to 10 percent and the slope by as much as 25 percent which is probably an upper limit to the systematic errors. The agreement of the rms derived from the PSF and Allan deviation, which removes a linear phase slope from the data, suggests that instrumental phase drifts are not a problem for shorter averaging times.

The averaging time is an important parameter. If one were only interested in the atmospheric statistics, then longer averaging times are required on longer baselines. However, the astronomer is more likely to be interested in how the phase varies with baseline for a fixed averaging time. The PSF provides an estimate of the error in the measured phase after a calibration interval corresponding to the averaging time. Tables 1 and 2 list the rms phase for various averaging times. Fixed averaging times will tend to underestimate β for the shorter averaging times. Indeed, the measured slope of the PSF does increase slightly with averaging interval.

The standard instrumental phase calibration at interval of 15 - 30 minutes suppresses fluctuations on longer time scales, and we will adopt 15 min as a standard averaging interval, in common with several recent studies. Published measurements of PSF's are summarized in Table 3. The measured phase noise has been converted to an rms pathlength at a 1 km baseline, using the β given in Table 3. The published phase noise and β are generally consistent with an rms path around 1mm at a 1 km baseline. The rms path ranges over an order of magnitude from 0.2 to 4mm. (Observers usually do not publish their worst data, so 4mm is lower limit)

The fitted power law slope, β, varies from 0.3 to 2, with the steeper slopes generally on the shorter baselines. Plots showing this trend from 2D to 3D turbulence (Wright & Welch, 1990; Masson 1994a), suggest that the break occurs around 100 to 300m. The break is not readily apparent in any of our data (see e.g. Figure 3), but if we fit the best sampled datasets between 14dec94 and 08feb95 we obtain an average β = 1.16 +/- 0.06 for baselines less than 300m (the median value); while for baselines between 300 and 846m we obtain β = 0.48 +/- 0.10. This result, using a 15min averaging interval may underestimate β on the long baselines. Using a 45min averaging interval, we obtain an average β = 1.18 +/- 0.21 for baselines less than 300m, and β = 0.58 +/- 0.10 for baselines between 300 and 846m. The two studies with the largest slopes (Armstrong and Sramek, 1982; Olmi & Downes, 1992) both used array baseline data comprised of several widely separated sources sampled for short intervals. The 3 dimensional nature of the sampling may result in a high β close to the Kolmogorov 3D value 5/3. Alternatively, the VLA data at 5 GHz (Armstrong & Sramek, 1982) may also suffer from ionospheric fluctuations which are readily apparent in VLBI data up to 10 GHz (Thompson, Moran & Swenson, 1986), and β=1.4 on Plateau du Bure at 86 GHz (Olmi & Downes, 1992) is consistent with the relatively short baselines sampled. On longer baselines, and in good weather, β tends towards 0.7 consistent with that expected for 2D Kolmogorov turbulence. A stable atmosphere over level ground is horizontally stratified with a capping inversion which varies in height from about 100m at night to 1-2 km by day (e.g. Kaimal & Finnigan, 1994). Most of the turbulence is expected to be within this Planetary Boundary Layer – PBL (Panofsky & Dutton, 1984), although mixing through the capping inversion has been cited (Coulman, 1991) as a possible mechanism for creating the large, anomalous refraction observed on radio telescopes at Pico Veleta (Altenhoff etal, 1987), and on Mauna Kea (Church

& Hills, 1990). A 10" refraction fluctuation observed with the JCMT telescope on Mauna Kea correponds to a 0.75mm path gradient across the 15m telescope; this is much larger than the fluctuations typically observed with interferometers on a 15m baseline. The large "anomalous" refractions correspond to the peak phase fluctuations seen in poor observing conditions at Hat Creek. As noted by Altenhoff etal. (1987), the more typical refraction fluctuations of 1 – 2" are consistent with the pathlength variations seen with interferometers.

Additional evidence for a thin turbulent layer or layers comes from the observed elevation dependence. For 3-dimensional turbulence the rms phase should scale approximately as $sin(elevation)^{-0.5}$, for 2-dimensional turbulence, as $sin(elevation)^{-1.0}$. For the 10 well sampled datasets between 14dec94 and 08feb95 we obtain an average elevation index 0.67 +/- 0.20 for baselines less than 300m, and 0.80 +/- 0.22 for baselines between 300 and 846m.

There is little direct evidence for a cutoff in the slope, even on baselines to 35 km (Sramek, 1990), and the rms phase continues to increase slowly to VLBI baselines (Wright & Welch, 1990). On baselines longer than the scale height of the water vapor, the dry atmosphere may contribute to the measured phase fluctuations. From an analysis of phase fluctuations in VLBI data, Rogers (1988) suggests that up to 30 percent of the fluctuations are from the dry component. There may also be a significant amount of turbulence in the upper atmosphere, perhaps associated with the diurnal breakup of the PBL, or with weather fronts (see, e.g. Coulman, 1991).

On short baselines or in turbulent weather, β approaches the Kolmogorov 3D value of $\beta = 5/3$. This case corresponds to summer afternoon conditions at Hat Creek when there are strong vertical thermal gradients, as evidenced by (latent) thunder storm activity, and winds 5 to 10 m/s. Only in these conditions do we observe the Kolmogorov value 5/3.

4.2. Taylor's Hypothesis

Taylor's hypothesis (Taylor, 1938) allows us to infer spatial structure from the temporal structure measured at one point, assuming that the turbulent pattern is frozen as it is blown across the array at the mean wind velocity. This powerful assumption allows us to compute the spatial PSF directly from the temporal PSF, and has been used, for example, to predict the PSF expected on prospective MMA sites from observations of water vapor temporal fluctuations (Holdaway, 1991). Support for Taylor's hypothesis comes from the consistency of the spatial and temporal statistics of wind fluctuations (Kaimal & Finnigan, 1994). From an analysis of the cross correlation of data obtained with the Cambridge One Mile Telescope Hinder (1972) found agreement with Taylor's hypothesis; in 80 percent of the data he analysed, the phase fluctuations were consistent with a turbulent pattern crossing the 3-antenna array with the wind velocity, the remaining 20 percent were not consistent with frozen turbulence. However, turbulence is neither frozen, nor transported at a uniform velocity. Many an unlucky sailor has watched a favourable gust crossing the water, only to find that it has re-arranged itself by the time it reaches his, or her, boat. We looked for evidence of coherent structures crossing the Hat Creek array. There is no apparent difference in the magnitude or frequency of the fluctuations parallel and perpendicular to wind, although the statistics obtained with a 6-antenna array are rather poor. The wind speed may increase above the surface layer 50-100m deep, but the direction is maintained over level ground (see e.g. Kaimal & Finnigan, 1994). Figure 2 shows a short run of data on the Orion SiO maser sampled at 2.3s intervals on 28jul95. The data were obtained in clear weather with wind speed 2 to 4 m/s from a direction 220 to 240 degrees. The rms phase is well fitted to $b^{0.8}$. The phase fluctuations are correlated across the array, but are not delayed in the wind direction as might be expected if there were a frozen turbulent pattern being blown across the array. A cross correlation analysis of the phase fluctuations shows multiple peaks, perhaps indicating several layers of frozen turbulence moving past the antennas at different velocities, but our data do not offer much support for the Taylor hypothesis. The anisotropy of the temporal phase fluctuations across the array favors a more isotropic distribution of velocity fluctuations. Studies of the transport velocities of turbulent eddies (Wilczak and Businger, 1984) show that large eddies move faster than small eddies, and that the average transport velocity is 0.7 to 0.8 times the mean wind velocity. In a convective atmosphere, or over hilly terrain, the vertical wind speed may exceed the horizontal component. Standing waves and strong wind shears (gradients) are not compatible with Taylor's hypothesis, which fails, for example, if the vertical wind shear, du/dz is greater than u/b, where u is the mean horizontal wind velocity, and b is the antenna separation.

On average there is a net transport of water vapor from the surface in order to balance precipitation. Turbulent eddies mix more humid air close to the surface with drier air above, and carry water vapor, and its latent heat energy, to higher altitudes. Much of the heat flux is transferred by convective plumes of hot air with diameters 100m (Kaimal, 1974); these do not satisfy Taylor's hypothesis (Davison, 1974). The water vapor is not well mixed with the dry component; large fluctuations can occur and are the probable cause of the anomalous refraction observed on Mauna Kea (Church & Hills, 1990).

Even if turbulence is not "frozen", the statistics of spatial and temporal fluctuations in the water vapor are coupled to those of the wind turbulence. In the analysis below we will assume Taylor's hypothesis is true in a statistical sense, i.e. $< b^2 >=< (vT)^2 >$, rather than $b = vT$, strictly proportional to the wind speed and direction, and we use the measured horizontal wind as indicative of the transport speed independent of direction. Table 4 lists the predicted slopes of various statistics for Kolmogorov-Taylor turbulence.

4.3. Allan deviations and phase power spectra

In Table 5 we compare the measured slopes for the PSF and Allan deviation for the best sampled data in the period 14dec94 to 08feb95. The PSF was computed for 15 minute intervals averaged over all the data. The Allan deviation was derived from $\sqrt{< (\phi(t-T) - 2\phi(t) + \phi(t+T))^2 >}$ averaged over each baseline for a time interval T. The Allan deviation removes linear phase drifts from the data. Figure 4 shows the Allan deviation for 21 Dec 1994. The slope of the

Allan deviation flattens at a time, T', 120 to 1300s. This "corner time", corresponds to the time for the turbulence to cross the baseline and is directly related to the "corner frequency" discussed by Masson (1994b). The measured corner times are commensurate with the baseline length and average wind speed, 2.2 m/s, but do not correlate in detail with the baseline and the wind speed, and no accounting has been attempted for wind direction, since similar corner times were seen independent of the measured wind direction with respect to the baseline orientation. The Allan deviation is a convenient measure of the coherence time for the interferometer, and sets an effective limit to the coherent integration time which can be used to avoid reducing the amplitude in the averaged data (see e.g. Rogers etal, 1984). The Allan deviation is commonly used to measure the fractional frequency stability of oscillators, $\delta f/f$. The Allan variance of the frequency stability, $\sigma_y(T)^2$, estimated from our atmospheric phase fluctuations is: $1/(2(\pi f T)^2) < (\phi(t-T) - 2\phi(t) + \phi(t+T))^2 >$, where f is the observing frequency, and T is the time interval, and assuming that the sampled data are contiguous (no dead time). The rms phase over a time interval, T is given by: $\sigma_A(T) = \sqrt(2)\pi f T \sigma_y(T)$. The slope of $\sigma_A(T)$ is listed in Table 5. The average slope , for times, T, less than the corner time is 0.43 +/- 0.02, in good agreement with the average slope of the PSF, $\beta/2$ = 0.45 +/- 0.02, but there is not a good correlation in detail, offering support for the Taylor hypothesis in a statistical sense only. The slope of the Allan deviation, defined above, is -0.57 for times less than the corner time. A similar slope is seen in 3mm VLBI data for averaging times 2 to 500s (Rogers etal, 1984). The slopes of the PSF and Allan deviation correspond to a spatial phase spectrum with index = 2.90 +/- 0.06, and 2.86 +/- 0.06 respectively, close to that expected for 2D turbulence (Tatarski, 1961; Armstrong & Sramek, 1982).

The phase power spectra were derived from Fourier transforms of contiguous data in each data set. Each baseline was analysed seperately. A sample of the power spectra obtained on 21 Dec 1994 are plotted in Figure 5. A flattening of the spectra below a corner frequency v/b is apparent in some baselines corresponding to the time for fluctuations to cross the array. The low frequency fluctuations which are evident probably result from uneven sampling and phase drifts in the data over a period of hours. The slope of the spectra above the corner frequency varies widely from about -1.2 to -2.1, with an average value -1.5 +/- 0.2. The corresponding spatial phase spectral index 2.5 +/- 0.2 is somewhat flatter than that derived from the PSF and Allan deviations. The difference can be understood in terms of the different transport velocity for large and small scale turbulence. Since large eddies move faster than small eddies, there is more power in fast time variations than would be expected if the turbulence was frozen.

4.4. Correlations with time, weather, and site

1. Seasonal, diurnal

We observe both seasonal and diurnal variations in both σ and β. The increase in σ in daytime (versus night), and summer observing is well known. We also observe an increase in β in conditions of high turbulence. The mean values for the winter (October to March), and summer (April to September) are: $\sigma_{15min}(1km) = 0.80 \pm 0.40$, and $\beta = 0.88 \pm 0.22$, and $\sigma_{15min}(1km) = 2.23 \pm 1.21$, and $\beta = 1.34 \pm 0.38$ respectively. Our statistics for diurnal variation are poor, but a diurnal variation in β was also noted at Plateau de Bure; at night $\beta = 1.11 \pm 0.02$, and by day $\beta = 1.85 \pm 0.04$ (Olmi & Downes, 1992). An increase in β is also suggested by the VLA data: summer daytime $\beta = 0.84$, nights = 0.74, winter days = 0.60, nights = 0.58 (see Sramek, 1990 - Table 1). The increase in turbulence is associated with an increase in the depth of the turbulent eddies, and hence in β.

2. Weather.

At Hat Creek we see in increase in both σ and β in turbulent weather, which may be exited by heat input, or by wind. (It is not clear from our data whether the wind stirs up larger eddies, or heat input creates both larger eddies, and stronger winds.) An increase in the humidity does not by itself lead to an increase in σ. At Cambridge, Hinder (1972), noted a correlation of σ with temperature (correlation coeficient, ρ = 0.58), with duration of sunshine (ρ = 0.46), and with cloud cover (ρ = -0.51), but no correlation with wind speed (ρ = 0.00). These results suggest that increased phase fluctuations are associated with convective activity.

3. Site Altitude, Topography.

The best rms path reported to date (Masson, 1994b) is at the highest altitude (4100m), and a general decrease in the average values of σ with site altitude is evident in Table 3. In Figure 6 we plot σ versus site altitude, extrapolating to a 1 km baseline using the published values of β. Better statistics for the variation of σ with altitude have been recently reported by Holdaway (1995) using satelite observations at 10 to 12 GHz on a 150m – 300m baseline at Nobeyama, Mauna Kea, and Chile. The data are consistent (with the usual caveats about extrapolating to longer baselines and millimeter wavelengths) with a decrease in σ with altitude, which is more shallow than the decrease in the total path – suggesting that the turbulent water vapor is in active layers, and not distributed though the total path; most likely at the top and bottom of the PBL (Lewellen, 1980).

A high altitude does not guarantee a low σ; 10" pointing errors due to anomalous refraction observed on Mauna Kea (Church & Hills, 1990), correspond to pathlength changes of 1mm over a distance of only 20m, moreover these large fluctuations can occur under conditions of low humidity, less than 1mm of precipitable water vapor, or 6mm of total path due to water vapor. Clearly, very large fractional fluctuations are possible under some conditions. The rms path is a larger fraction of the total path at higher altitudes. In the case of the anomalous refraction reported at Pico Veleta at 2850 m altitude (Altenhoff etal, 1987), and at JCMT at 4100m altitude (Church & Hills, 1990), the fluctuations require that a large fraction of the water vapour be in the form of a gradient, or wedge, over the telescope which causes the observed pointing errors. At the highest altitudes there is insufficient water vapor to support large rms fluctuations in stable atmospheric conditions. The site topography is also important. We might expect that some fraction of the turbulence in the water vapor is injected into the PBL from ground effects (see, e.g. Kaimal & Finnigan, 1994). The atmospheric phase fluctuations will then depend on the details of the array configuration and the local topography; there is increased turbulence, for example, in the lee of a hill, and the highest wind velocities are experienced at the crest of a hill. Certainly we might expect more variations in the phase fluctuations measured across the complex topography of Mauna Kea than across a large open site such as the VLA, or the proposed MMA site in Chile. Taylor's hypothesis may be more valid on a large open site (large compared to the size of the telescope array) than in hilly terrain.

4.5. Atmospheric Phase Correction

Methods to correct for atmospheric phase fluctuations can be divided into two classes : 1) direct measurement of the phase shift along the same or adjacent path through the atmosphere. 2) measurement of some related quantity such as the water vapour, or total power variations along a line of sight to, or close to the source. Several methods have been explored, and are discussed at length by Holdaway and others (1992a, 1992b, 1995). In the following formulation we do not assume that the turbulence is frozen, since there is little direct evidence for this in our data; rather we assume that both the spatial structure and the temporal variations can be described by a phase structure function, with the spatial and temporal variations adding in quadrature.

4.6. Standard Phase Calibration

The standard calibration technique is to alternate observations of the source with short observations of a nearby quasar or other compact source at intervals of 5 to 50 minutes in order to calibrate the instrumental phase versus time. The phase of the calibrator is interpolated and subtracted from the measured source phase. This calibration corrects for a slowly varying instrumental phase offset, and reduces geometrical errors, Δb, by $\Delta b.(s - s_0)$, where $\vec{s}$ and $\vec{s_0}$ are unit vectors in the directions of the source and calibrator, respectively. The choice of calibrator and calibration interval is a compromise between SNR and calibration errors (e.g. Wright, 1991); a stronger calibrator will give better SNR in a shorter interval, but the stronger calibrator is typically located further from the source, resulting in larger geometric errors. The standard calibration also reduces the slowly varying part of the atmospheric phase fluctuations. The effective distance between the source and the calibrator is given by $d = \sqrt{(h(s - s_0))^2 + (v\Delta T)^2}$ where h is the height of the turbulence in the direction of the source, and v the mean turbulent velocity over an interval ΔT. Both source and calibrator suffer atmospheric phase fluctuation given by the phase structure function $D\phi(b) = \langle(\phi(x + b) - \phi(x))^2\rangle$, where b is the interferometer baseline. After calibration, the phase fluctuations will be reduced if $d < b$. This analysis is similar to that presented by Holdaway (1992b), but does not assume a frozen turbulence drifting past the antennas.

Consider the following examples. Assume $h = 2$ km, a source-calibrator separation = 10 degrees, $v = 10$ m/s, and $\Delta T = 15$ minutes. These parameters imply $h(s - s_0) = 350$ m and $v\Delta T = 9$ km. Thus standard calibration will not reduce atmospheric phase fluctuations on baselines less than about 9 km. To reduce the atmospheric phase fluctuations on shorter baselines, a shorter calibration interval should be used. The situation is improved if the velocity of the turbulence is smaller, say $v = 1$ m/s. In these conditions, and with a shorter calibration interval, $\Delta T = 5$ minutes, $v\Delta T$ is 300 m, comparable to the term $h(s - s_0)$, then atmospheric phase fluctuations will be reduced on baselines longer than about 460 m. An additional improvement is expected if the turbulence is closer to the antennas, i.e. h is smaller.

4.7. Fast Switching

Atmospheric phase fluctuations can be reduced by rapidly switching between the source and a nearby calibrator. The effect has been nicely demonstated at the VLA site using a source - calibrator separation of 2 degrees, and a switching time of 40s. The residual phase fluctuations after calibration increased with baseline to about 400m, and then remained constant (Holdaway & Owen, 1995). Using the above analysis, this is consistent with a mean turbulent velocity of about 7 m/s. Holdaway & Owen assume Taylor's hypothesis, and derive 10 m/s. At Hat Creek, we made several tests of fast switching between the bright quasars 3c273 and 3c279, with angular separation 10.4 degrees

In summer conditions (August 1994 and July 1995), when the atmospheric turbulence is extremely high, the data are consistent with an increase in rms phase on short baselines ($d > b$), and a reduced rms on long baselines ($d < b$)) after calibration. For the 28 July 1995 data, with baselines ranging from 8 to 86 m, using 3c273 to calibrate 3c279 with a 30 second switching interval (including a 10s integration on one source), reduced the fitted PSF slope from 1.5 (close to the Kolmogorov 3D value) to 0.6. The fitted rms phase at a 1 km baseline was reduced from 387 to 111 degrees. The rms phase on baselines less than about 50 m was increased after calibration; on baselines 50–86 m, the rms phase was only slightly reduced, but an improvement by a factor of more than 3 would be obtained at 1 km because of the flatter slope. Using a calibration interval longer than 60s increased the phase noise on all baselines. The flattening of the phase structure function between 50 and 100m is consistent with upper limits to the turbulence height and velocity of about 500m, and $1 - 2$ m/s respectively. Using the actual measured wind velocity (4 ± 1 m/s), we would expect to see a constant rms phase on baselines longer than about 100 m. Unfortuately our longest baseline in summer was 86 m. In winter with baselines to 800m, a repeat of these fast switching experiments did not lead to the expected improvement on longer baselines. Evidently the atmospheric conditions may vary considerably; the winter experiments imply that $d = \sqrt{(0.18h)^2 + (30v)^2}$ was greater than 800m. In summer, the strong thermal gradients create considerable ground level turbulence, and it is reasonable to expect that much of the turbulent water vapor is close to the ground and can be calibrated by switching to a nearby calibrator on 30s time scales. In winter, most of the turbulence may be higher and moving faster and is not removed on 30s time scales. Further experiments are needed with faster switching and closer calibrators. There is a compromise between a weak calibrator close to the source, and a more distant, stronger calibrator which could allow a faster switching cycle. Analysis of atmospheric phase fluctuations in Hat Creek baseline data shows that the rms does not increase rapidly with source separation, suggesting that much of the atmospheric turbulence is close to ground, with h less than about 300m. A similar result was obtained at the VLA by Sramek (1983) for source–calibrator separations 6–23 degrees. Analysis of radiometer opacity fluctuations at South Baldy (altitude 3200m) (Holdaway, 1991) also suggest that the phase structure function has a turnover at a few hundred m., suggesting that the turbulent layer is only a few hundred m thick.

Clearly, faster switching is desirable. Our fast sampled data shows phase fluctuations on 1s. time scales. The switching speed is limited by both hardware and software. At Hat Creek the measured resonant frequency of the antennas is 3 – 4 Hz in both azimuth and elevation axes. An efficient slew over a few degrees can be achieved in 3 – 4 s, but the data aquisition software currently limit the minimum switching time to about 30s, with a 10s integration on source.

4.8. Self Calibration

In self calibration we estimate the complex antenna gains (amplitude and phase) at each antenna, g_i from a model of the source visibilities v'_{ij} by minimizing $\sum_{ij}[(g_i g_j v_{ij} - v'_{ij})/\sigma_{ij}]^2$ over time intervals ΔT. The model visibilities are usually obtained iteratively from an image of the source distribution (e.g. Cornwell and Fomalont, 1989). The estimated antenna phases, including atmospheric phase fluctuations on timescales greater than ΔT, are used to correct the data and make a better image. The conditions for convergence, and the noise introduced into the image by the errors in the estimated antenna phases are discussed by Cornwell and Fomalont. The noise in the estimated gains depends on ΔT. If ΔT is too small then the image quality is limited by the errors, σ_G, in the estimated antenna gains; if ΔT is too long then the image quality is limited by atmospheric phase fluctuations. The optimum self calibration interval depends on the source flux density and baseline length. Cornwell and Fomalont show that σ_G is approximately $\sigma_v/(S\sqrt{N})$ where σ_v is the thermal noise on each baseline, S is the source flux density, and N the number of antennas. The atmospheric phase noise in an averaging interval ΔT increases with ΔT up to a maximum given by the phase structure function, $D\phi(b)$. The thermal noise decreases as $\sqrt{(}\Delta T)$. The optimum self calibration interval is obtained where the phase noise from the estimated gains and from the atmosphere are equal. The atmospheric phase fluctuations, after self calibration, are given by $D\phi(d)$, where d is the rms value of $(v\Delta T)^2)$ over the self calibration interval ΔT and v is the mean velocity of the turbulence. Atmospheric phase fluctuations on baseline b will be reduced if $v\Delta T$ is less than about $4b$.

At millimeter wavelengths, several spectral lines can often be observed simultaneously. The source structure can change, both within one spectral line as a function of frequency, and also from one spectral line to another. Since the source flux density may be distributed over many channels, a multichannel model is required in the self calibration. The instrumental frequency response must be calibrated, and removed from the data before a multichannel self calibration, or before applying the antenna gains determined for one spectral line to other frequency bands. Another extension of self calibration which is relevant at millimeter wavelengths is to determine the antenna gains from several nearby fields as in a mosaic observation. These options have been programmed into the MIRIAD software (Wright and Sault, 1993), and have been used to good advantage to calibrate weak spectral line, or continuum emission using self calibration on a strong spectral line which is observed simultaneously (e.g. Wright et al.,1995; Plambeck et al. 1995). For wide bandwidth multichannel observations (e.g. MFS synthesis, Conway etal, 1990), a further improvement to the self calibration algorithm would be to determine the antenna gains as functions of the observing frequency, f, since the phase is expected to vary as $f\tau_w + f^{-2}\tau_i$, where τ_w is the tropospheric fluctuation (due mainly to water vapor), and τ_i is the ionospheric fluctuation. If the data contain simultaneous observations of millimeter and centimeter wavelengths, then the antenna gains can be used to determine both τ_w and τ_i. Even if the data are all at short wavelengths where the ionopheric delay is negligible, the fractional bandwidth may be quite large, and it would be better to scale the atmospheric delay with frequency, rather than apply the antenna phase directly over a wide frequency range.

4.9. Simultaneous Observation of Source and Calibrator

If the source is not strong enough for self calibration on a time scale short compared with atmospheric phase fluctuations, another possibility is to simultaneously observe both the source and a nearby calibrator. This might be achieved by having a subset of the antennas observe the calibrator whilst the remaining antennas observe the source. Consider a pair of antennas, one looking at the source, the other at the calibrator. The effective separation between the source and the calibrator is given by $d = \sqrt{(h(s - s_0))^2 + (b')^2}$ where b' is the baseline between these two antennas. After calibrating the source using the calibrator phase observed on the paired antenna, the phase fluctuation will be given by $D\phi(d)$; atmospheric phase fluctuations will be reduced if d is smaller than b, where b is the baseline being calibrated. Clearly, to work well the array configuration should consist of pairs of antennas with small separations compared with the the baselines being used for the source observations. Using a smaller number of antennas to observe the calibrator increases d, and hence increases the residual phase fluctuations after calibration. Instrumental phase offsets between the antennas can be removed by alternating source and calibrator observations on all antennas. The source and the calibrator need not be observed at the same frequency provided that the instrumental frequency response is properly accounted for in the calibration. A more detailed analysis of paired antenna configurations (howbeit assuming Taylor's hypothesis) is given by Holdaway (1992b). Since only half the array is used to observe the source at one time, the number of baselines ($N(N-1)/2$, where N is the number of antennas) is greatly reduced, and the paired antenna scheme is rather unattractive.

4.10. Measurements of Atmospheric Water Vapor

At millimeter wavelengths both atmospheric emission, and pathlength variations are dominated by water vapor. Since the real and imaginary parts of the water vapor refractivity are related through the Kramers-Kronig relation, we might be able to correct for the atmospheric path length variations by measuring the atmospheric brightness fluctuations in the direction of the radio source. Near the 22.2 GHz water line the path length variation with the brightness temperature of the emission is about 21 mm/K. The emission varies inversely with pressure, so that water vapor at high altitude causes less path length change per K than at low altitude. At 20.6 GHz in the line wing, the path length per K brightness is nearly independent of the height of the water vapor (Westwater, 1967; Thompson, Moran & Swenson, 1986). Liquid water droplets in clouds also emit strongly, but cause little path length change. Measurement of the brightness temperature at two or more frequencies enables estimates to be made of both water vapor and droplets. A JPL water vapor radiometer at 20.7 and 31.4 GHz was able to determine the atmospheric pathlength due to water vapor to 2.5 mm rms (Resch, Hogg, and Napier, 1984). The increased accuracy required for millimeter wavelength interferometry has led to renewed efforts to build better water vapor radiometers at the 22 GHz water line at OVRO, and at 183 GHz at JCMT.

At an observing frequency away from the water lines, the emission from atmospheric water vapor is optically thin. In clear weather, assuming that all the water is in the form of water vapour, a measurement of the brightness temperature fluctuations gives a direct measurement of the integral, or column density, of water vapor in the direction of the radio source. The corresponding path length variation is about 1.6mm/K at 100 GHz, and 0.3mm/K at 250 GHz (Welch, 1994). Although the same receiver can be used for both observations and water vapor measurements, the brightness temperature of the atmosphere must be measured to an accuracy of 0.01 K in order to measure 2 degrees of atmospheric phase shift at 100 GHz. For a typical (current) system temperature of 200 K, and a bandwidth of 1 GHz, the thermal noise allows this accuracy in an integration time 0.2 s, i.e. fast enough to follow the atmospheric fluctuations. However, the gain stability needed, 10^{-4}, requires careful attention to the thermal and mechanical stability of the receiver components, and the total powers on each antenna must be accurately calibrated (Plambeck etal. 1996). Two of the BIMA antennas were recently retro-fitted with receivers with the required gain stability. Figure 7 shows a plot of the phase and total power difference between these two antennas during a test run with this new system. The phase and total power fluctuations track closely with a correlation coeficient 0.86 (Figure 8), and slope 2.5 mm/K, about 20 percent larger than the predicted value. Only an offset, corresponding to a difference in system temperature, has been removed from the total power since we wish to correct the phase using the total power difference. There is little doubt that the total power fluctuations correspond to atmospheric emission. The total power fluctuations on each antenna are about 100 times larger on the sky than observed on an ambient temperature load, and each follows a structure function with time with a power law slope β=0.8, consistent with our measured phase structure function. The two antennas were separated by only 43m, and the total power fluctuations on each antenna are nearly identical with a correlation coeficient 0.997. The total power difference plotted in Figure

7 does not perfectly track the interferometer phase. Correcting the interferometer phase by the measured atmospheric emission using the fitted slope, reduces the rms phase from 74 degrees to 34 degrees, a significant reduction in terms of the dynamic range in aperture synthesis images. The corresponding amplitude loss factor due to decorrelation, $e^{-\phi_{rms}/2}$, improves from 0.43 to 0.84. There are several possible reasons why the slope and the correlation might vary with atmospheric conditions. Since the slope (mm/K) varies with the altitude of the water vapor, multiple layers of turbulence at different altitudes will reduce the correlation between path length (phase) and emission. In particular, water vapor close to the ground, and close to the inversion layer may account for most of the turbulence (Lewellen, 1980. - see his Figure 15). Aggregates of water vapor, dimers, and polymers up to $n = 10^6$ may cause variations in absorption up to $50 percent$ (Gebbie, 1980). Thus it may be necessary to calibrate the slope of the correlation between path length and brightness temperature fluctuations (mm/K) quite often. This can be done from observations of a standard calibrator at intervals. There is also the problem of interpolating the absolute system phase from the predicted atmospheric phase fluctuations which must be applied on times scale commensurate with the fluctuations , i.e. less than a few seconds; shorter than the usual integration and data dump times. One possible solution is to apply the predicted phase rate to each antenna from the measured emission change, dK/dt, and to calibrate the total system phase using the corrected average value of the calibrator phase which is observed at intervals. This procedure has the benefit of existing antenna hardware to set the phase rate (fringe rate generators and the like).

5. CONCLUSIONS

1) Measurements of atmospheric phase fluctuations on a 1km baseline show rms pathlength variations of 1mm on 10s timescales at millimeter wavelengths. The standard phase calibration is inadequate; modified observing and data reduction procedures are required for aperture synthesis at millimeter wavelengths on long baselines.

2) The PSF follows a power law with slope $\beta = 0.7$ in good weather, consistent with 2D turbulence. A β close to the Kolmogorov slope 1.67 for 3D turbulence is observed only on short baselines, and in turbulent weather. The variation of β, and the elevation dependence of the PSF suggest turbulent regions 100 - 300 m thick. Although similar rms and β are measured at other sites, there is evidence that the fluctuations decrease at high altitude under stable weather conditions.

3) The measured rms phase can vary by factor 4, even in good weather - this requires flexible scheduling for efficient observing.

4) Both rms and β increase with wind speed. The atmospheric phase fluctuations may be more closely associated with, and increase with, convective activity, rather than being in a frozen turbulent pattern transported over the array. At Hat Creek we have seen little direct evidence for any dependence of phase fluctuations with wind direction, and derive an expression for combining temporal and spatial dependence in quadrature. Taylor's hypothesis for frozen water vapor

fluctuations may be more valid at other sites, but this remains to be demonstrated.

5) Self calibration techniques which remove the atmospheric phase fluctuations can greatly improve the data. At millimeter wavelengths a modified self calibration to handle multiple channels and pointing centers is valuable, since the source flux density may not be concentrated in a few bright regions. Fitting atmospheric delay, rather than the phase, at each antenna is also desirable for wideband multichannel and MFS synthesis. Although self calibration is very successful for strong sources, it can lead to spurious results for weak sources with small arrays of antennas, and other methods of correcting for atmospheric phase fluctuations must be developed for aperture synthesis at millimeter wavelengths.

6) Fast switching between a source and a nearby calibrator can reduce the rms phase on baselines longer than few hundred meters. Switching times of a few seconds are desirable, but lead to high data rates for multichannel data.

7) Predictions of the atmospheric delay from measurements of the atmospheric water vapor emission show that it may be possible to correct the data in real time on short times scales. Further development of these techniques is needed.

8) If a combination of fast phase switching, and phase correction from water vapor measurements is able to correct for atmospheric phase fluctuations, so that phase coherent aperture synthesis images can be obtained using baselines of several km, then longer coherent integration times can also used for millimeter VLBI, resulting in better sensitivity. Phase coherent VLBI images should also be possible with sub-milliarcsec resolution.

6. Acknowledgements

The Hat Creek array is operated by the Berkeley, Illinois, Maryland Association, supported in part by NSF Grant AST 93-20238. The author thanks the referee, Colin Masson, for many helpful comments, and for sharing his insights on corner frequencies and the like, Jack Welch, Don Backer and Dick Plambeck for helpful conversations, and David Wilner for a careful reading of an early draft of the manuscript.

REFERENCES

Altenhoff,W.J., Baars, J.W.M., Downes,D., and Wink,J.E., 1987, A&A 184, 381.

Armstrong,J.W., & Sramek,R.A., 1982, Radio Science 17,1579.

Baldwin, J.E, & Wang Shouguan, 1990, IAU symp on Radio Astronomical Seeing, Permagon Press, Oxford.

Bester,M, Danchi,W.C., Degiacomi,C.G., Greenhill,L.J., & Townes,C.H. 1992, ApJ, 392,357.

Bieging,J.H., Morgan,J., Welch,W.J., Vogel,S.N., & Wright,M.C.H.,1984, Radio Science 19,1505.

Church,S.E. & Hills, R.E., 1990, IAU symp on Radio Astronomical Seeing, J.E.Baldwin and Wang Shouguan (eds). p.75

Conway,J.E., Cornwell,T.J, and Wilkinson,P.N., 1990, MNRAS, 246, 490.

Coulman, C.E., 1991, A&A 251, 743.

Coulman, C.E., and Vernin,J., 1991, Applied Optics 30, 118.

Cornwell,T.J., and Fomalont,E.B., 1989, Synthesis Imaging in Radio Astronomy. ed. R.A.Perley, F.R.Schwab, and A.H.Bridle, ASP Conf. Ser. 6, 185.

Davison,D.S., 1974, Quart.J.Roy.Meteor.Soc., 100, 572.

Gebbie,H.A., 1980, in Atmospheric water vapor, A.Deepak, T.D.Wilkerson, and L.H.Ruhnke (eds), Academic Press, New York. p. 133.

Hinder,R., & Ryle,M., 1970, Nature, 225, 614.

Hinder,R., & Ryle,M., 1971, MNRAS 154, 229.

Hinder,R., 1972, J. Atmos. and Terrestrial Phys., 34, 1171.

Holdaway, M.A., 1991, NRAO. Millimeter Array Memo 68.

Holdaway, M.A., 1992a, NRAO. Millimeter Array Memo 84.

Holdaway, M.A., 1992b, NRAO. Millimeter Array Memo 88.

Holdaway, M.A., 1995, NRAO. Millimeter Array Memo preprint.

Holdaway, M.A. and Owen, F.N., 1995, NRAO. Millimeter Array Memo 126.

Ishiguro,M., Kanazawa,T., and Kasuga, T., 1990, in IAU symp on Radio Astronomical Seeing, J.E.Baldwin and Wang Shouguan (eds), p.60.

Kaimal,J.C., 1974, Quart.J.Roy.Meteor.Soc., 100, 46.

Kaimal,J.C., & Finnigan,J.J., 1994, Atmospheric Boundary Layer Flows, OUP, Oxford.

Kasuga,T., Kanzawa,T., and Ishiguro,M., 1986, IEEE Trans. Antennas Propagation, AP-34, 797.

Kasuga,T., Kanzawa,T., and Ishiguro,M., 1990, in IAU symp on Radio Astronomical Seeing, J.E.Baldwin and Wang Shouguan (eds), p.54.

Kolmogorov,A.N., 1941, Doklady, ANSSSR 30, 301

Lewellen,W.S., 1980, in Atmospheric water vapor, A.Deepak, T.D.Wilkerson, and L.H.Ruhnke (eds), Academic Press, New York., p.527.

Masson,C.R., 1994a. in IAU on Very High Angular Resolution Imaging 1-10. J.G.Robertson and W.J.Tango (eds).

Masson,C.R., 1994b. Astronomy with Millimeter and Submillimeter Wave interferometry, M.Ishiguro and Wm.J.Welch (eds), ASP conference series 59, 87

Olmi, L. & Downes, D., 1992, A&A 262, 634.

Plambeck, R.L., Wright, M.C.H., Mundy, L.G., & Looney, L.W. 1995, ApJ, 455, 189

Plambeck et al. 1996, in preparation.

Panofsky, H.A. & Dutton, J.A., 1984, Atmospheric Turbulence, Wiley, New York.

Rogers,A.E.E, Moffet,A.T., Backer,D.C., and Moran,J.M., 1984, Radio Science 19,1552.

Rogers,A.E.E., 1988, IAU symposium 129, p533.

Resch,G.M., Hogg,D.E., and Napier, P.J., 1984, Radio Science 19, 411.

Sramek,R.A., 1983, NRAO VLA Test Memo 143.

Sramek,R.A., 1990, in IAU symp on Radio Astronomical Seeing, J.E.Baldwin and Wang Shouguan (eds). p.21.

Tatarski,V.I.,1961,Wave Propagation in a Turbulent Medium, McGraw-Hill,New York.

Taylor, G.I., 1938, Proc Roy Soc (London) Ser A, 164, 476.

Thompson, A.R, Moran, J.M., & Swenson, G.W. Jr., 1986, Interferometry and Synthesis in Radio Astronomy, Wiley, New York.

Welch, W.J., 1994. Astronomy with Millimeter and Submillimeter Wave interferometry, M.Ishiguro and Wm.J.Welch (eds), ASP conference series 59, 1

Westwater, E.R., 1967, ESSA Tech report IER 30-ITSA 30, Boulder, Colorado.

Wilczak,J.M., and Businger,J.A., 1984, J.Atmos. Sci. 41, 3551.

Wright, M.C.H, & Welch, W.J., 1990, in IAU symp on Radio Astronomical Seeing, J.E.Baldwin and Wang Shouguan (eds). page 71.

Wright,M.C.H., 1991 BIMA memo 19 - Optimized Calibration

Wright,M.C.H., & Sault,R.J., 1993, ApJ, 402, 546.

Wright, M.C.H., Plambeck, R.L., Mundy, L.G., & Looney, L.W. 1995, ApJ, 455, 185

This preprint was prepared with the AAS LaTeX macros v4.0.

Table 1: Rms path (mm) at 1 km and slope versus physical baseline

—	5 min		15 min		45 min		135 min	
date	sigma	slope	sigma	slope	sigma	slope	sigma	slope
07nov93	0.11	0.36	0.13	0.26	0.26	0.22	0.44	0.14
20nov93	0.21	0.49	0.18	0.32	0.21	0.21	0.62	0.25
25dec93	0.55	0.68	0.63	0.69	0.74	0.66	0.75	0.58
27jan94	0.28	0.41	0.36	0.41	0.49	0.45	0.74	0.58
10apr94	1.31	0.62	1.72	0.66	2.52	0.75	1.79	0.61
14dec94	0.78	0.47	1.09	0.52	1.31	0.44	2.35	0.36
15dec94	0.43	0.30	0.66	0.43	1.03	0.52	2.15	0.69
20dec94	0.89	0.26	1.37	0.35	1.98	0.33	3.27	0.39
21dec94	0.62	0.36	0.86	0.48	1.46	0.62	1.93	0.52
25dec94	0.57	0.43	0.81	0.56	1.27	0.76	1.56	0.63
28dec94	0.82	0.27	1.33	0.38	1.96	0.34	2.17	0.36
01jan95	0.79	0.36	1.12	0.42	1.75	0.48	3.66	0.59
02jan95	0.52	0.40	0.82	0.51	1.59	0.93	2.31	0.73
07feb95	0.53	0.41	0.68	0.43	1.10	0.57	1.80	0.64
08feb95	0.75	0.31	1.18	0.38	1.58	0.38	2.34	0.45
15aug95	2.33	0.64	3.65	0.58	—	—	—	—
17aug95	1.02	0.77	2.69	0.95	—	—	—	—
18aug95	0.66	0.61	0.86	0.51	—	—	—	—

Table 2: Rms path at 1 km, slope, and elevation dependence.

—	5 min			15 min		
Date	sigma	slope	elevation	sigma	slope	elevation
07nov93	0.08	0.36	-0.86	0.13	0.26	-0.42
20nov93	0.15	0.51	-0.74	0.18	0.33	-0.54
25dec93	0.50	0.71	-0.65	0.63	0.70	-0.58
27jan94	0.23	0.44	-0.92	0.32	0.44	-0.79
10apr94	1.38	0.65	-1.13	1.33	0.68	-1.24
14dec94	0.70	0.46	-0.67	1.06	0.53	-0.55
15dec94	0.34	0.29	-0.84	0.47	0.40	-0.94
20dec94	1.37	0.28	0.09	2.12	0.37	0.09
21dec94	0.36	0.31	-1.19	0.39	0.38	-1.51
25dec94	0.42	0.43	-1.01	0.56	0.45	-0.88
28dec94	0.83	0.27	-0.48	1.36	0.38	-0.47
01jan95	0.82	0.36	-0.44	1.23	0.44	-0.38
02jan95	0.32	0.37	-1.27	0.52	0.47	-1.27
07feb95	0.62	0.43	-0.29	0.81	0.45	-0.28
08feb95	1.27	0.34	0.32	1.95	0.42	0.27

Table 3: Published Structure function Measurements

baseline	frequency [GHz]	rms path [mm]	slope [β]	Reference
1.6 km	5	0.7 - 2.6	1.3	Hinder and Ryle, 1971
1 - 35km	5	1.0	1.4	Armstrong and Sramek, 1982
100m - 3km	22	0.6	0.72	Sramek, 1983
12 - 150m	86	1.2	1 - 2	Bieging etal, 1984
27 - 540m	22	0.5 - 0.9	1.6	Kasuga etal, 1986
50m - 35km	5/15	0.6 - 1.6	0.6 - 0.8	Sramek, 1990
35m	19	1.9	1.2	Ishiguro etal, 1990
6 - 100m	86	0.7 - 1.0	1.1 - 1.4	Wright and Welch, 1990
1 - 1200km	100	0.7	0.3 - 0.6	Wright and Welch, 1990
24 - 288m	86	0.3 - 0.7	1.1 - 1.9	Olmi and Downes, 1992
100m	12	0.2 - 1	0.4 - 2	Masson, 1994
6 - 846m	86	0.8 - 2.2	0.8 - 1.3	This paper.

Table 4: Predicted slopes for Kolmogorov - Taylor turbulence

Statistic		3D turbulence	2D turbulence
3D spatial power spectrum	α	3.67	2.67
Structure Function [β]	α -2	1.67	0.67
Temporal phase spectrum	1- α	-2.67	-1.67
Allan deviation	0.5 α -2	-0.17	-0.67
rms from time series	0.5 α -1	0.83	0.33

Table 5: Comparison of Slopes derived from Phase Structure function and Allan deviation

Date	Structure function	Allan deviation	Comment	Wind speed [m/s]
14dec94	0.52	0.50	break at 200s.	1.52 (0.95)
15dec94	0.43	0.50	break at 150s.	1.75 (1.29)
20dec94	0.43	0.40	break at 500s.	0.93 (0.85)
21dec94	0.48	0.50	break at 120s.	1.05 (0.94)
25dec94	0.56	0.35	break at 700 s.	1.31 (1.23)
28dec94	0.38	0.40	break at 1300s.	6.49 (4.09)
01jan95	0.42	0.42	break at 400s.	2.68 (2.10)
02jan95	0.51	0.45	break at 200s.	0.88 (0.77)
07feb95	0.43	0.45	break at 630s.	1.33 (0.91)
08feb95	0.38	0.34	break at 800s.	4.53 (1.91)

7. Figure captions

Figure 1. The interferometer phase for the Orion SiO maser with antenna separations from 97 to 846 m. The phases are plotted with respect to antenna 4.

Figure 2. This shows a well defined atmospheric phase event during a short run of data on the Orion SiO maser sampled at 2.3s intervals on 28 July 1995. The antennas are located at 0, 30m, and 72m west, 30m, and 42m north respectively with respect to a reference antenna at 12m east.

Figure 3. The Phase Structure Function for 21 December 1994. Each point represents a 15min sample of the data from which an rms phase was calculated.

Figure 4. The Allan Deviation for 21 December 1994. The curves show the variation of the rms phase as a function of the time interval between sampled points. The points for each baseline are connected and identified as follows: 1) 70m, 2) 140m, 3) 80m, 4) 160m, 5) 110m, 6) 160m, 7) 260m, 8) 330m, 9) 400m, a) 370m, b) 460m, c) 520m, d) 580m, e) 600m, f) 240m.

Figure 5. Temporal Phase Power Spectra for 21 December 1994. Each panel plots the power spectra for contiguously sampled data. The projected baseline length is indicated for each panel.

Figure 6. RMS pathlength versus site altitude. A range of values is plotted corresponding to winter and summer averages (Cambridge – 17m; Hat Creek – 1035m; Nobeyama – 1350m), winter and summer, day and night (VLA – 2124m), night and day (IRAM – 2550m), and for a range of β (Mauna Kea – 4100m). References as in Table 3.

Figure 7. Interferometer phase and total power difference between two antennas separated by 43m.

Figure 8. Correlation between Interferometer phase and total power difference between two antennas separated by 43m.

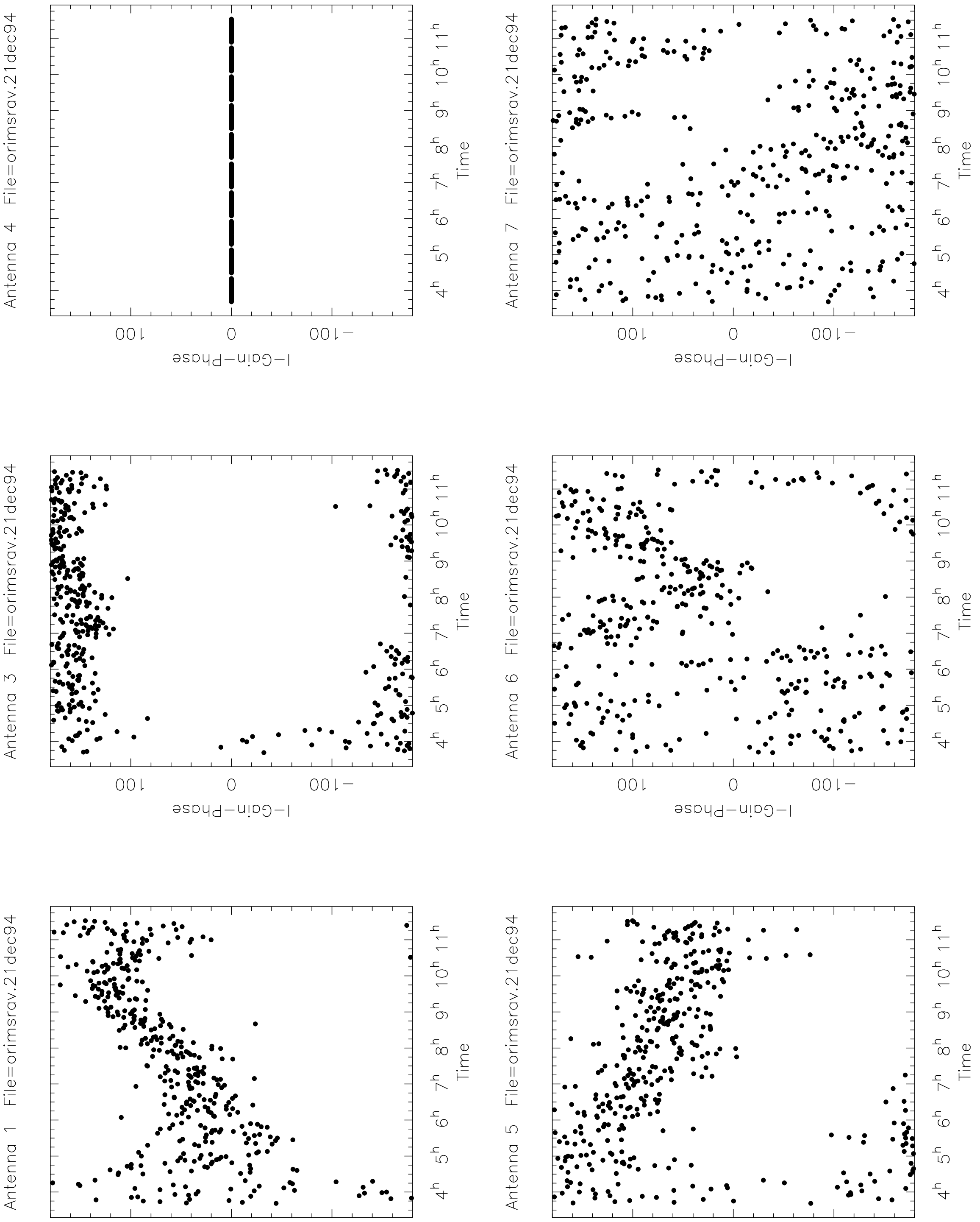
Antenna 1 File=orimsrav.21dec94
Antenna 3 File=orimsrav.21dec94
Antenna 4 File=orimsrav.21dec94
Antenna 5 File=orimsrav.21dec94
Antenna 6 File=orimsrav.21dec94
Antenna 7 File=orimsrav.21dec94
I–Gain–Phase
Time
100
0
−100

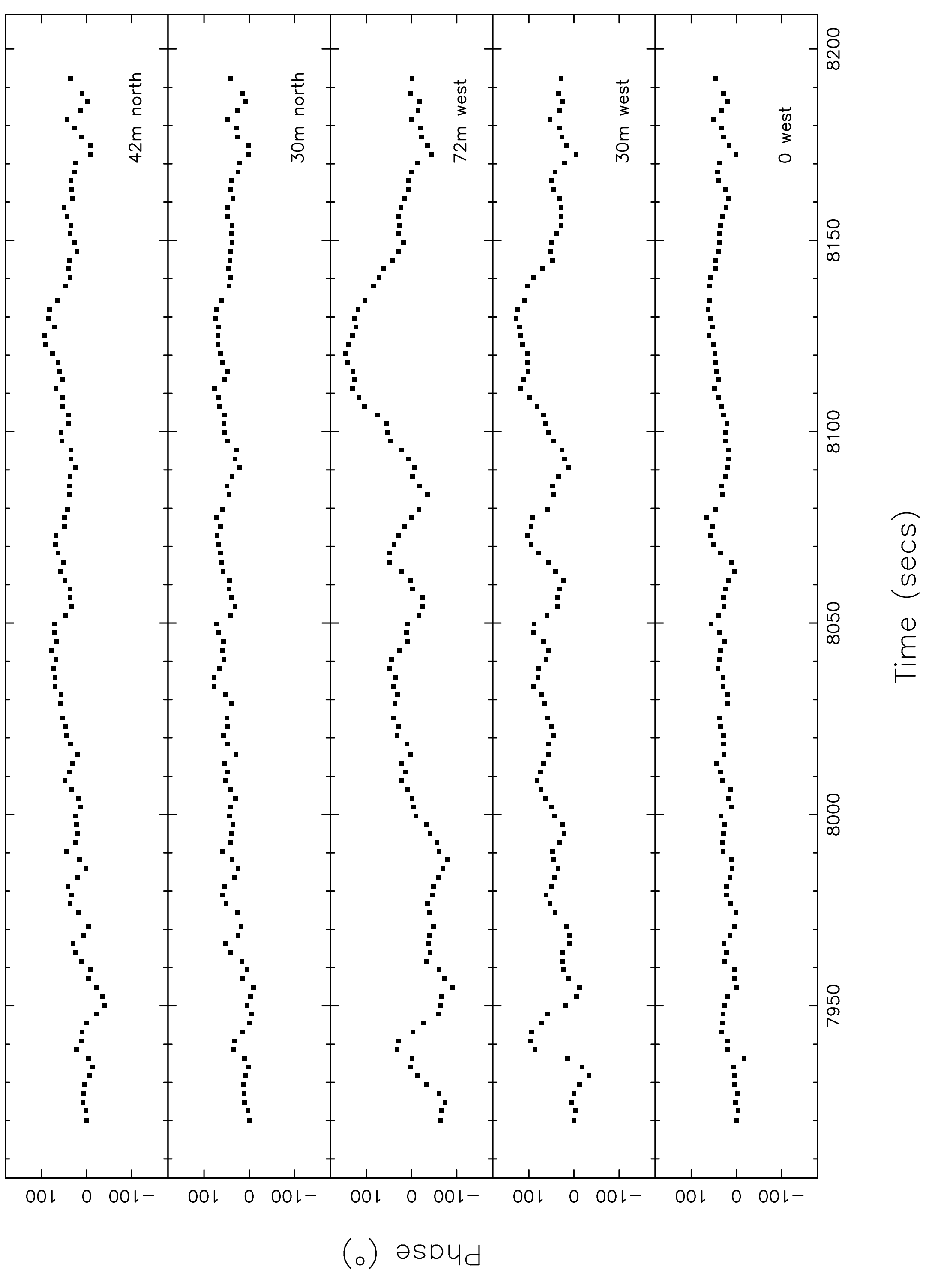
42m north
30m north
72m west
30m west
0 west
Time (secs)
Phase (°)
7950
8000
8050
8100
8150
8200
100
0
−100

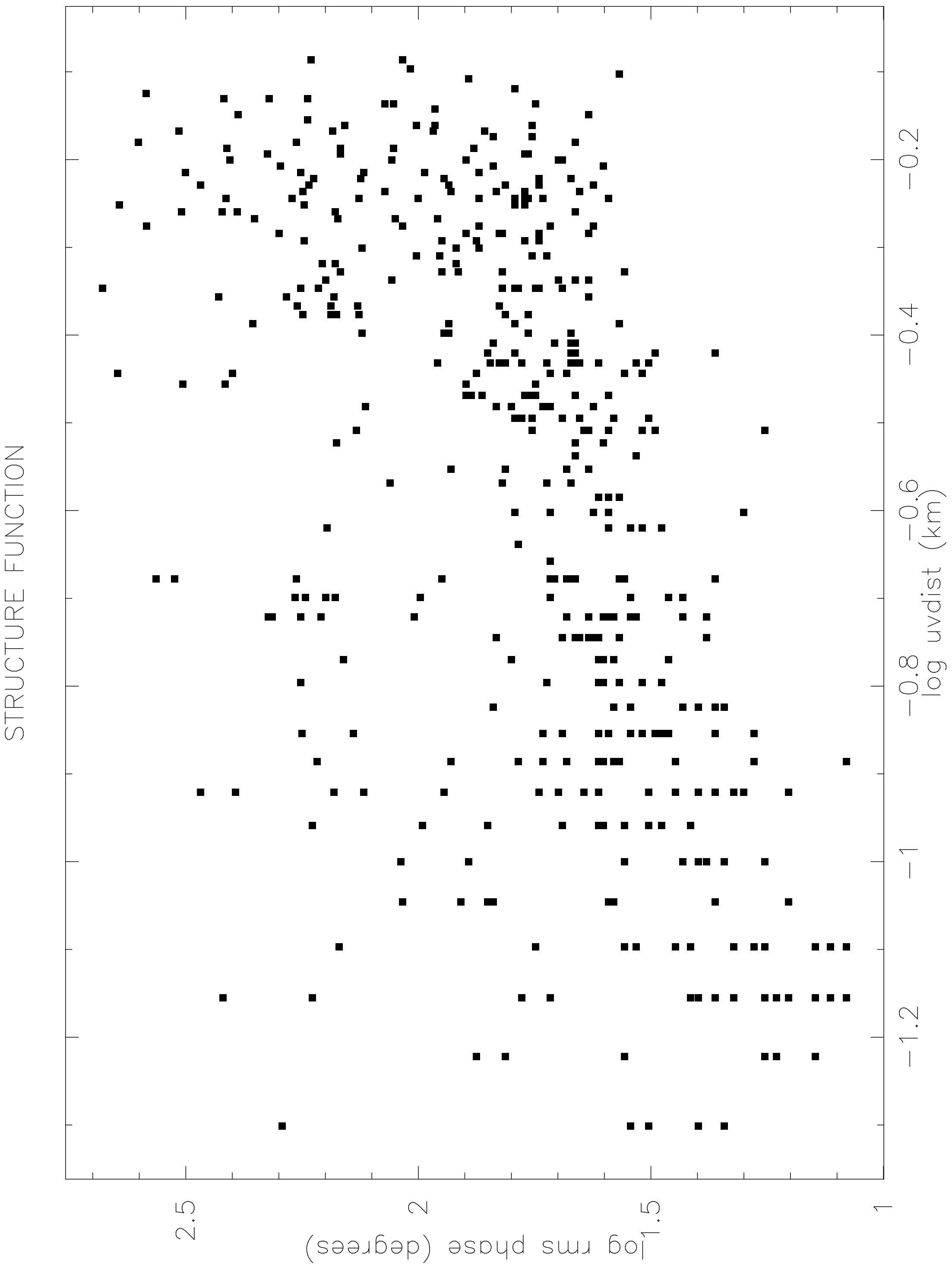
STRUCTURE FUNCTION
log uvdist (km)
−1.2
−1
−0.8
−0.6
−0.4
−0.2
log rms phase (degrees)
2.5
2
1.5
1

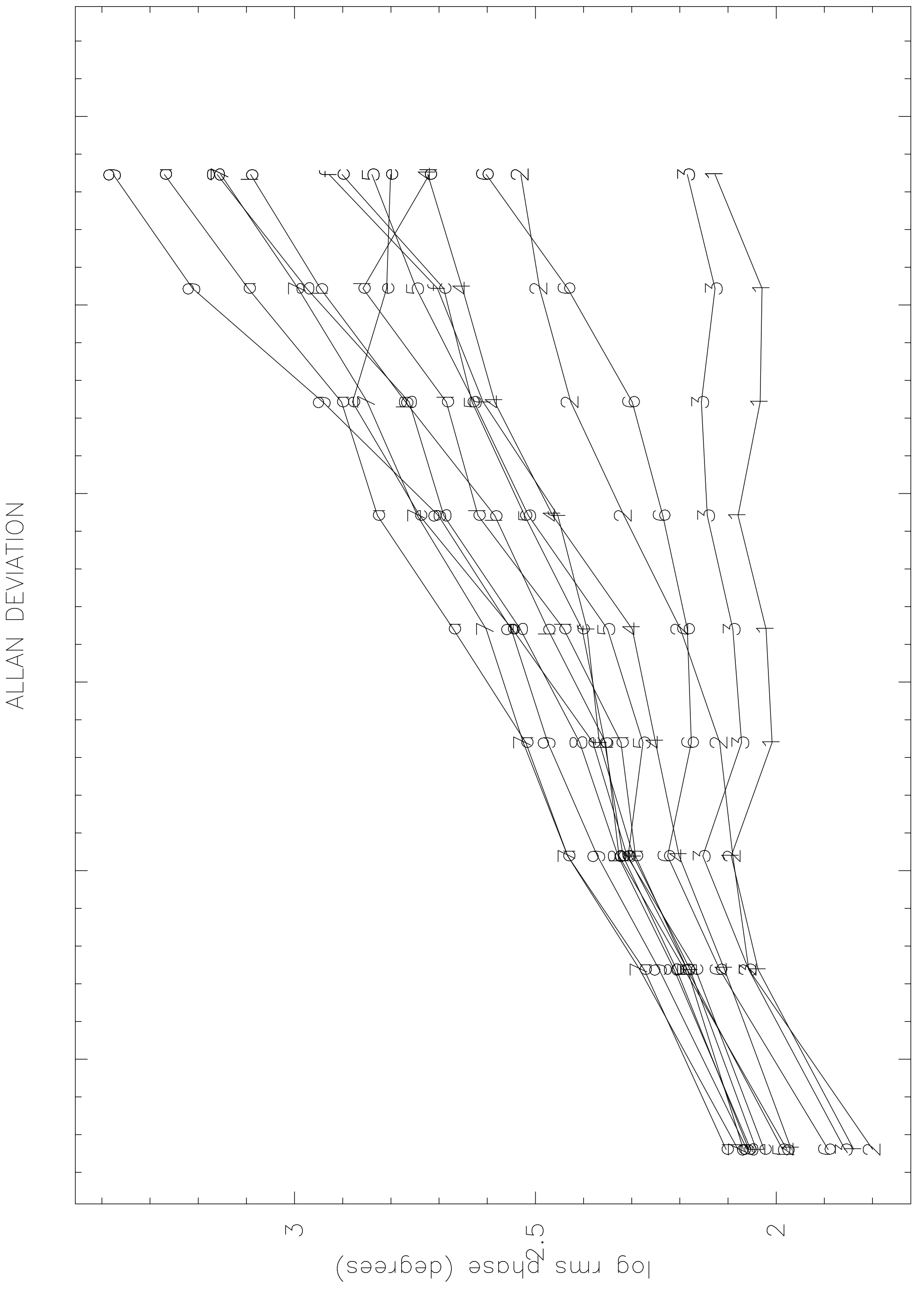
ALLAN DEVIATION
log time interval (seconds)
log rms phase (degrees)
1.5
2
2.5
3
3.5
4
2
2.5
3

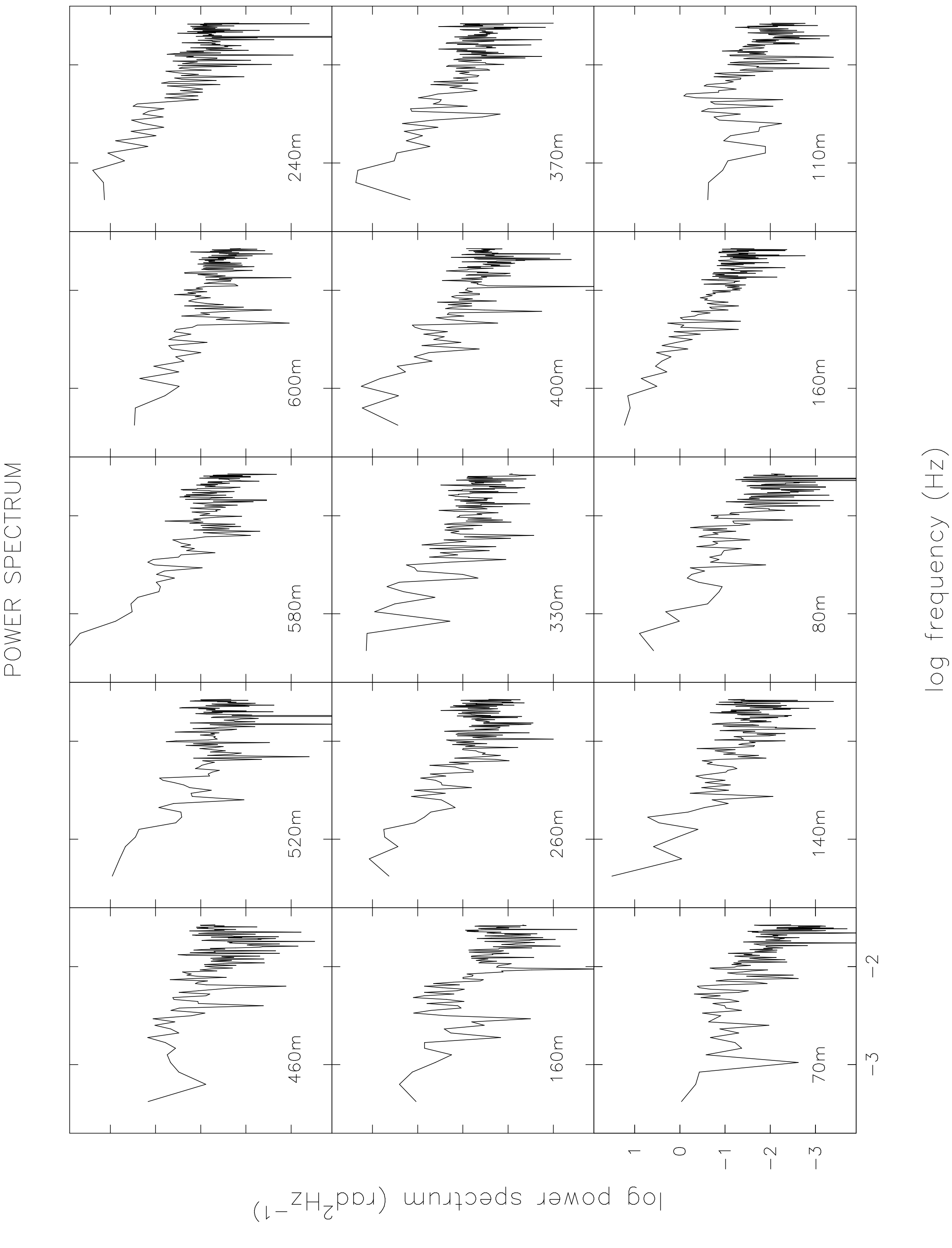
POWER SPECTRUM
460m
520m
580m
600m
240m
160m
260m
330m
400m
370m
70m
140m
80m
160m
110m
−3
−2
log frequency (Hz)
1
0
−1
−2
−3
log power spectrum (rad^{2}Hz^{-1})

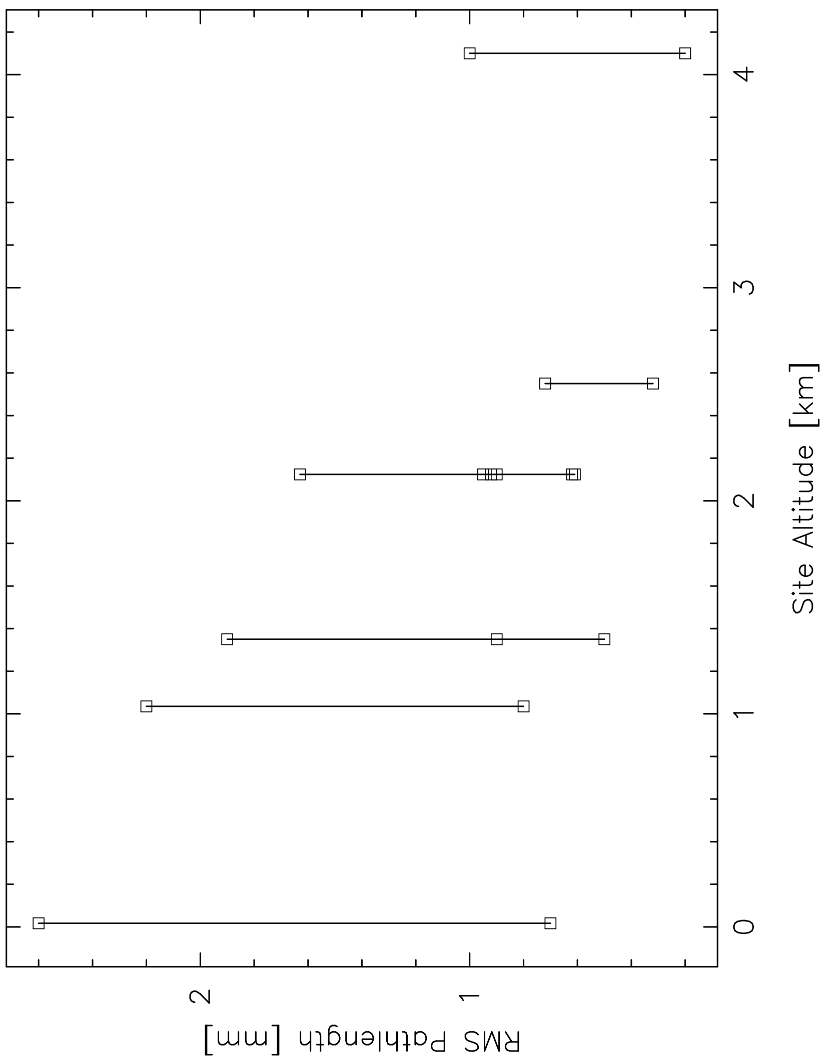
RMS Pathlength [mm]
Site Altitude [km]
0
1
2
3
4
1
2

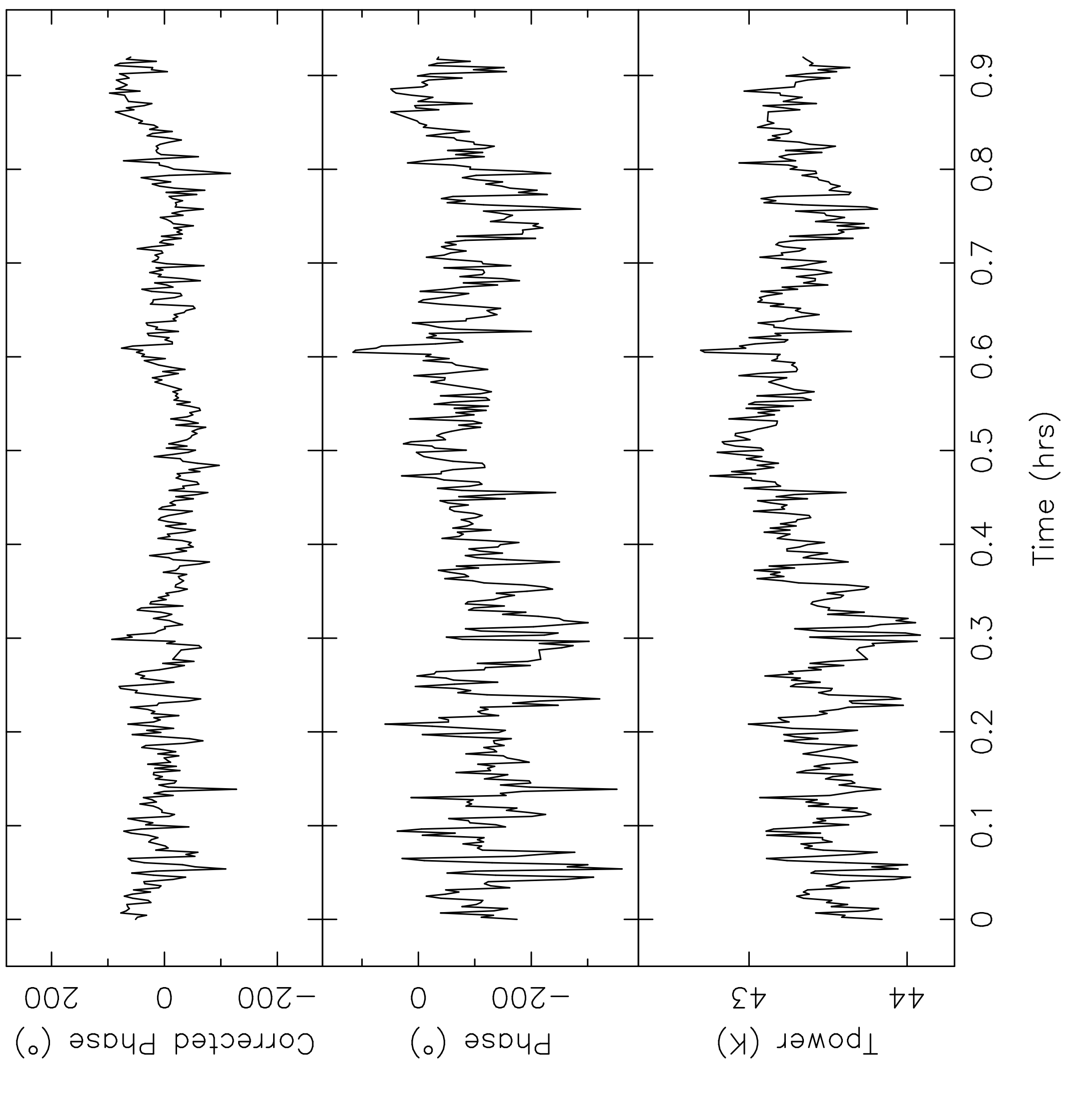
Corrected Phase (°)
Phase (°)
Tpower (K)
Time (hrs)

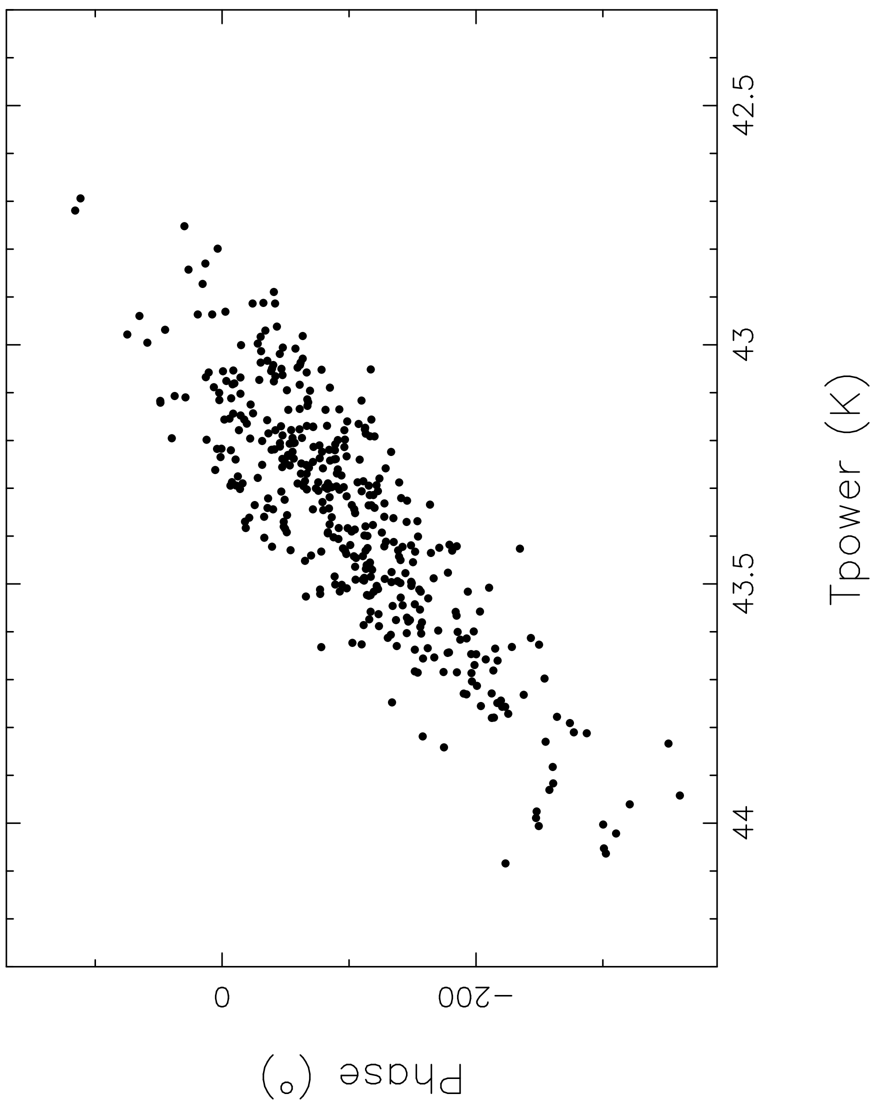
Tpower (K)
Phase (°)
42.5
43
43.5
44
0
−200